Draft version July 26, 2018
Preprint typeset using LATEX style emulateapj v. 12/16/11

arXiv:1807.09361v1 [astro-ph.SR] 24 Jul 2018

BROAD NON-GAUSSIAN Fe XXIV LINE PROFILES IN THE IMPULSIVE PHASE OF THE 2017 SEPTEMBER 10 X8.3–CLASS FLARE OBSERVED BY *HINODE*/EIS

Vanessa Polito
Harvard-Smithsonian Center for Astrophysics, 60 Garden Street, Cambridge MA 01238, USA

Jaroslav Dudík, Jana Kašparová, and Elena Dzifčáková
Astronomical Institute of the Czech Academy of Sciences, Fričova 298, 251 65 Ondrejov, Czech Republic

Katharine K. Reeves and Paola Testa
Harvard-Smithsonian Center for Astrophysics, 60 Garden Street, Cambridge MA 01238, USA

Bin Chen
Center for Solar-Terrestrial Research, New Jersey Institute of Technology, Newark, NJ, United States

Draft version July 26, 2018

ABSTRACT

We analyze the spectra of high temperature Fe XXIV lines observed by *Hinode*/EIS during the impulsive phase of the X8.3–class flare on September 10, 2017. The line profiles are broad, show pronounced wings, and clearly depart from a single Gaussian shape. The lines can be well fitted with κ distributions, with values of κ varying between ≈1.7 to 3. The regions where we observe the non-Gaussian profiles coincide with the location of high-energy (≈100–300 keV) HXR sources observed by *RHESSI*, suggesting the presence of particle acceleration or turbulence, also confirmed by the observations of a non-thermal microwave sources with the *Expanded Owens Valley Solar Array* (EOVSA) at and above the HXR looptop source. We also investigate the effect of taking into account κ distributions in the temperature diagnostics based on the ratio of the Fe XXIII 263.76 Å and Fe XXIV 255.1 Å EIS lines. We found that these lines can be formed at much higher temperatures than expected (up to $\log(T\,[\mathrm{K}]) \approx 7.8$), if departures from Maxwellian distributions are taken into account. Although larger line widths are expected because of these higher formation temperatures, the observed line widths still imply non-thermal broadening in excess of $200\,\mathrm{km\,s^{-1}}$. The non-thermal broadening related to HXR emission is better interpreted by turbulence rather than chromospheric evaporation.

Keywords: Sun: activity - Sun: flares - techniques: spectroscopic - line: profiles - radiation mechanisms: non-thermal - Sun: UV radiation

1. INTRODUCTION

Solar flares (e.g., Fletcher et al. 2011; Schmieder et al. 2015) are bright manifestations of the release of magnetic energy via the process of magnetic reconnection, leading to plethora of observed dynamics. From the viewpoint of spectroscopy, one of the long-standing problems is the presence of broad profiles of flare lines, usually interpreted in terms of non-thermal (turbulent) velocities (e.g., Doschek et al. 1979, 1980; Feldman et al. 1980; Culhane et al. 1981; Antonucci et al. 1982, 1986; Antonucci 1989; Tanaka et al. 1982; Landi et al. 2003; Del Zanna et al. 2006; Milligan 2011; Brosius 2013; Young et al. 2013; Tian et al. 2014; Polito et al. 2015, 2016; Bamba et al. 2017; Lee et al. 2017; Woods et al. 2017). Typically, the largest non-thermal velocities, of the order of 100–200 $\mathrm{km\,s^{-1}}$, are observed in the hottest flare lines available, such as Fe XXI–Fe XXVI. Such high non-thermal broadenings occur exclusively during the start or the impulsive phases of a flare, followed by a decrease to about 60 $\mathrm{km\,s^{-1}}$ during the gradual phase. Reports of much smaller velocities of ≈40 $\mathrm{km\,s^{-1}}$ in the impulsive phase have been also made (Young et al. 2015, Table 2 therein) using the Fe XXI line observed by the *IRIS* satellite (De Pontieu et al. 2014). Progressive broadenings, from about 40 to 90 $\mathrm{km\,s^{-1}}$ have been also reported during the rise phase of a long-duration X1-class flare (see, e.g., Sect. 3.2 and Fig. 10 of Dudík et al. 2016). If the broad flare line profiles are interpreted in terms of the equivalent (Doppler) ion temperatures, values above 100 MK can be obtained (e.g., Antonucci et al. 1986; Antonucci 1989), which are almost an order of magnitude higher than the corresponding electron temperatures of several 10^7 K at which the hot flare lines are formed.

For the sake of completeness, we note that non-thermal broadening of EUV lines of the order of several tens of $\mathrm{km\,s^{-1}}$ are found also outside flaring regions, such as in the active region transition region and corona (e.g., De Pontieu et al. 2015; Brooks & Warren 2016; Testa et al. 2016). Further, large non-thermal velocities are not found exclusively in flares, but can also be found in microflares, where they can also reach 145 $\mathrm{km\,s^{-1}}$ (Brosius 2013, Table 2 therein).

Recently, Jeffrey et al. (2016, 2017) showed that the shape of the broad line profiles during flares can deviate from a single Gaussian. In particular, non-Gaussian wings were observed in the Fe XVI and Fe XXIII lines with the Extreme-Ultraviolet Imaging Spectrometer (EIS, Culhane et al. 2007) onboard the *Hinode* spacecraft (Kosugi et al. 2007). These line profiles were fitted by the non-Maxwellian κ-distributions (Olbert 1968; Vasyliunas 1968a,b; Livadiotis & McComas 2009; Livadiotis 2017; Dudík et al. 2017b), yielding low values of κ ($\approx$ 2–3), which indicate strong departures from the Gaussian shape. We note that similar findings were obtained for active region brightenings in transition-region lines (Dudík et al. 2017a), as well as coronal holes (Jeffrey et al. 2018). Jeffrey et al. (2017) found that the flare line profiles described by a κ-distribution could occur either due to ion acceleration or presence of turbulence. This is not surprising, since turbulence leads naturally to enhanced high-energy tails of the particle distributions, if the turbulent diffusion coefficient is inversely proportional to velocity (Hasegawa et al. 1985; Laming & Lepri 2007; Che & Goldstein 2014). In flares, such situation can lead to a κ-distribution (Bian et al. 2014). The high-energy tails can, however, be also produced by particle acceleration (e.g., Gordovskyy et al. 2013, 2014; Gontikakis et al. 2013) or wave-particle interaction involving whistler waves, as shown by Vocks et al. (2008, 2016).

The κ-distributions of electrons have been suggested in flares using the *RHESSI* (Lin et al. 2002) spacecraft. The method consisted of fitting the X-ray bremsstrahlung spectra, which allows to determine the κ index for the high-energy tail (Oka et al. 2013, 2015) or the entire spectrum (Kašparová & Karlický 2009). Alternatively, the κ parameter can be determined by combining observations from the *RHESSI* spacecraft and the Atmospheric Imaging Assembly (AIA, Lemen et al. 2012; Boerner et al. 2012) onboard the *Solar Dynamics Observatory* (*SDO*, Pesnell et al. 2012) using the mean electron flux spectrum (Battaglia & Kontar 2013; Battaglia et al. 2015). Yet another method involves the ratios of emission line intensities which are formed over a wide range of energies of the impacting electrons that produce ionization and excitation. Such method have been used to detect strongly non-Maxwellian κ-distributions in the rise and impulsive phase of the X5.4–class solar flare of 2012 March 07 (Dzifčáková et al. 2018).

In this work, we report on detection of strongly non-Gaussian and broad line profiles of Fe XXIV at the top of the flare loops during the strongest solar flare of the Solar cycle 24, i.e., the X8.3–class Flare of 2017 September 10. This is a limb flare, allowing for localizing the non-Gaussian profiles from a different viewpoint than the on-disk flares of Jeffrey et al. (2016, 2017). The paper is organized as follows. Section 2 describes the spectroscopic observations used and their reduction. Fitting of the line profiles is detailed in Sect. 3 and the results on temperature diagnostics based on the Fe XXIV 255.10/Fe XXIII 263.76 Å ratio is discussed in Sect. 4. Section 5 describes the analysis of the *RHESSI* spectra and fitting of the various spectral components. The results obtained are discussed in Sect. 6 and a summary is given in Sect. 7.

2. OBSERVATIONS

The X8.3 flare under study occurred on September 10, 2017 in the AR $\beta\gamma$ NOAA 12673 on the west limb of the Sun. The flare started at ≈15:40 UT and peaked at about 16:06:28 UT, as observed by the *GOES* satellite in the 1–8 Å filter (see Fig. 1). Several authors have focused on the analysis of this event, which was observed simultaneously by different satellites, including *SDO*, *Hinode*, *IRIS*, *RHESSI*, and *Fermi* (e.g., Warren et al. 2018; Long et al. 2018; Seaton & Darnel 2018; Yan et al. 2018; Li et al. 2018). The flare was initiated by a fast eruption of a flux rope cavity starting at about 15:54UT. It was also associated with increase in non-thermal electron energy flux as measured by *Fermi* (see Fig. 1 in Long et al. 2018). Spectroscopic observations performed by *Hinode*/EIS were studied in Warren et al. (2018) and Li et al. (2018), who focused on studying the evolution of the hot plasma in a plasma sheet formed after the fast eruption and above the flare loops, from Solar-X coordinates ≈960″ towards larger solar radii (see Fig. 2).

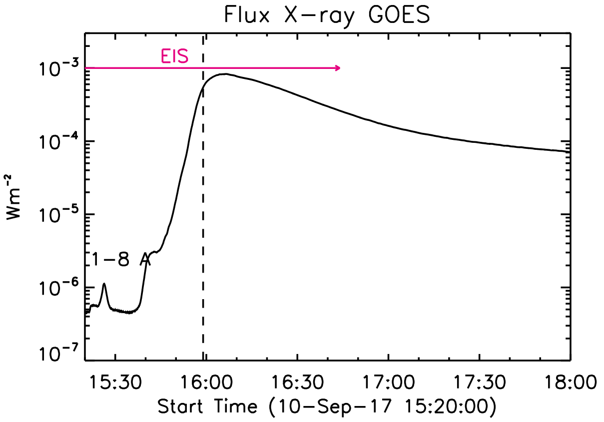

Figure 1. *GOES* soft X-ray light curve in the 1–8 Å channel for the X-class flare on September 10, 2017. The pink arrow indicates the duration of the EIS observation under study (which starts at 05:44 UT). The horizontal dotted line shows the time where we observe the non-Gaussian Fe XXIV line profiles.

In this work, we focus on analyzing the profiles of the high temperature lines observed by *Hinode*/EIS (Fe XXIV and Fe XXIII) in the plasma sheet at around 15:59 UT, as indicated by the horizontal line in Fig.1. We note that Warren et al. (2018) and Li et al. (2018) focused on the EIS spectra observed after 16:09 UT, i.e., towards the peak and gradual phases of the flare. At these times, the Fe XXIV and Fe XXIII lines could be well-fitted by Gaussians (see, e.g., Figure 2 in Li et al. 2018 and Figure 10 in Warren et al. 2018). Long et al. (2018) studied the EIS spectra associated with the fast eruption at about 15:42 and 15:54 UT (see their Figures 3 and 4). Our analysis is complementary to these ones both in time and as well as because of its different focus on the non-Gaussian shape of line profiles.

The analysis of the EIS spectra is complicated by some well-known technical issues (as summarized in the EIS wiki page[1]), some of which are briefly described in Sect. 2.1. We use high-resolution *SDO*/AIA images (0.6″ per pixel) in the 193 Å filters, which provide an essential context for the spectroscopic observations and useful information on the plasma emission measure (see Sect. 4). The level 1.5 AIA data were processed using the *SolarSoft* (SSW; Freeland & Handy 1998) routine

---

[1] http://solarb.mssl.ucl.ac.uk/eiswiki/Wiki.jsp?page=EISAnalysisGuide

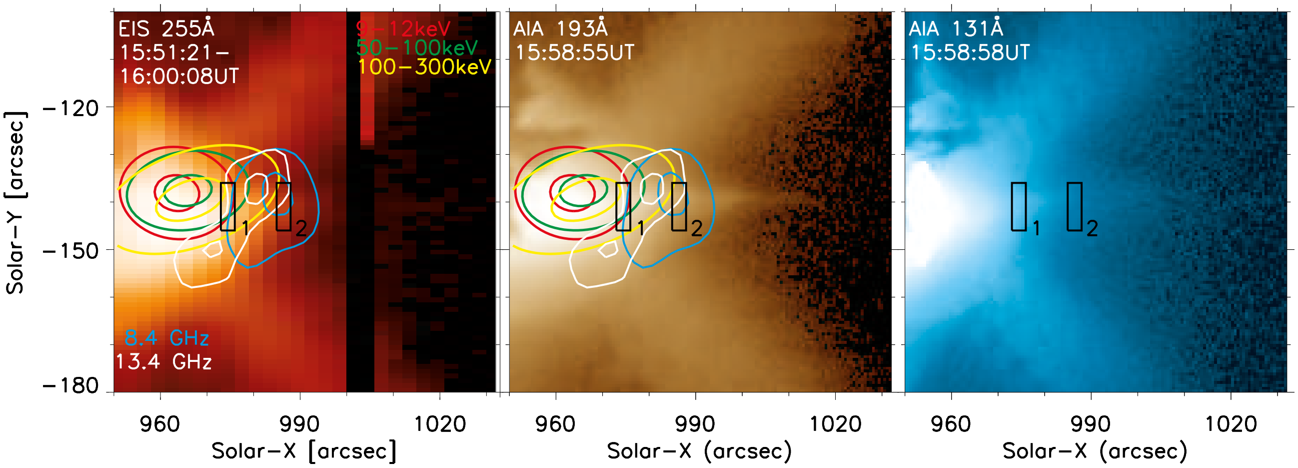

Figure 2. Overview of the 10th September 2017 flare observation with *Hinode*/EIS and *SDO*/AIA. *Left panel:* Intensity image formed in the Fe XXIV 255.10 Å line during one of the EIS rasters (from 15:51:21 to 16:00:08 UT), obtained by performing a single Gaussian fit at each raster pixel. *Middle and right panels:* AIA 193 Å and 131 Å images at the closest time to the EIS raster exposures number 8–9. The colored contours in the left and middle panels show the 50 and 90% of the maximum intensity of the HXR sources observed by *RHESSI* during the time interval 15:58:40–15:59:40 UT, and the microwave sources observed by *EOVSA* between 15:59:08 UT and 15:59:12 UT, with different colors indicating different energy intervals as shown in the legend. Finally, the black boxes 1 and 2 indicate the location where we perform the κ fitting of the Fe XXIV 255.10 Å (raster exposures 8–9) and 192.03 Å (raster exposures 12–13) lines respectively.

`aia_prep.pro`, which corrects for instrumental pointing errors and co-aligns images from different filters on a common platescale. We also analyzed hard X-ray (hereafter, HXR) images from the *RHESSI* satellite, whose data reduction is discussed in Sect. 5. The flare was also observed in microwave wavelengths in 2.5–18 GHz by the Expanded Owens Valley Solar Array (*EOVSA*). An overview of the *EOVSA* observations is provided by Gary et al. (2018).

2.1. *EIS data reduction and instrumental issues*

On September 10, 2017 EIS observed the AR 12673 while running a large 80-step raster from 05:44 UT to 16:44 UT, covering all the impulsive and part of the gradual phase of the X8.3–class flare (see Fig. 1). For each raster, the 80 2″ slit positions were separated by a 1″ jump, resulting in a 3″ raster step and field-of-view for the spectrometer of 240″ x 304″. The exposure time was 5 s, and the total duration of each raster was ≈535 s. The EIS study consisted of 15 spectral windows, which included 3 high temperature lines that are only observed during flares: Fe XXIII 263.76 Å ($\log(T\,[\mathrm{K}])\approx 7.15$), Fe XXIV 192.03 and 255.10 Å ($\log(T\,[\mathrm{K}])\approx 7.2$). The Fe XXIII 263.76 Å line is believed to be largely free of blends, whereas the Fe XXIV 192.03 Å and 255.10 Å lines are contaminated with unidentified emission at 1 MK, as well as other lines including Fe XI, Fe XII, Fe XVII (Del Zanna 2008, 2012), especially if the width of the Fe XXIV lines is large. Nevertheless, during flares, Fe XXIV appears to be the dominant contribution (Del Zanna 2008).

The level 0 EIS data were converted to level 1 datacubes (λ, X-pixels, Y-pixels) by using the `eis_prep.pro` routine with some of the standard options [2] , including the keyword `refill` to interpolate the missing pixels. We note that the interpolation is a necessary step because of the large number of missing pixels in this observation. According to the EIS Software Note 13, the interpolation works well since the EIS spatial resolution is 3–4 pixels in the Solar Y direction. This means that a signal within a given pixel contains a significant component from the neighboring spatial element. We also note that the interpolation of EIS spectra is a standard procedure before non-Gaussian fitting (see Section 4.7 of Jeffrey et al. 2016, also Jeffrey et al. (2017, 2018)). However, in some cases our profiles still show 1 or 2 missing pixels which could not be interpolated by `eis_prep.pro`. Finally, because of the uncertainty in the EIS radiometric calibration and its evolution (see, e.g. Del Zanna 2013; Warren et al. 2014), we use the `/noabs` keyword in `eis_prep.pro` and obtain the spectra in data number (DN).

We estimated an offset of about 16.5 pixels between the short-wavelength (SW, including the Fe XXIV 192.03 Å line) and long-wavelength (LW, including the Fe XXIV255.10 Å line) CCD channels by using the routine `eis_ccd_offset.pro`. Although we took into account this offset when co-aligning spectra from the two CCDs, for simplicity the spectra are labelled with their original ”uncorrected” pixel position. We also note that because of the offset between the two CCDs and the fact that the instrumental width varies with the CCD Y-pixel position, this latter will be different for lines which are included in different CCD channels, such as the Fe XXIV 192.03 Å and the 255.10 Å (or Fe XXIII 263.76 Å) line. This difference needs to be taken into account when fitting the line profiles, as discussed in Sect. 3. Further, we correct for the spectral tilt by using the SSW routine `eis_slit_tilt_array.pro`.

Finally, Warren et al. (2018) pointed out the effects of the EIS assymmetric PSF, which causes apparent red and blueshifts in the centroid of the Fe XXIV line (and other bright lines) on either sides of the plasma sheet for the flare under study (see Fig. 12 of Warren et al. 2018). We note that this instrumental effect does not influence the results of our analysis, as we observe Fe XXIV spec-

---

[2] ftp://sohoftp.nascom.nasa.gov/solarsoft/hinode/eis/doc/eis_notes/01_EIS_PREP/eis_swnote_01.pdf

tra with pronounced wings in several locations across the plasma sheet in the direction perpendicular to its length. In addition, if this effect was responsible for creation of the non-Gaussian wings, it should be seen in other conditions, for example in the same lines at different times. This is not the case, as these strong lines become Gaussian after 16:09 UT (Li et al. 2018; Warren et al. 2018).

3. FITTING OF THE Fe XXIV AND Fe XXIII LINES

Mostly symmetric Fe XXIV line profiles with pronounced wings were observed at several locations along the plasma sheet feature during the EIS raster which was running between 15:51 UT and 16:00:08 UT. Figure 2 (left panel) shows the intensity map of the EIS Fe XXIV 255.10 Å line during this raster, which has been obtained by performing an approximate single-Gaussian fit at each pixel location. We note that the EIS slit rasters from right to left, and therefore the intensity map is actually a composite image obtained at different times. The profiles that we analyze in this work are observed in boxes 1 and 2 (shown in Figure 2), whose locations correspond respectively to the X-pixels 8–9 and 12–13 of the EIS datacube. Boxes 1 and 2 are located above the loop tops, at the bottom and along the plasma sheet structure respectively. The right panel shows the AIA 193 Å image at ≈15:59 UT, which is the approximate time where the EIS slit was rastering the location indicated by box 1. Overlaid on both images on left and right panels are the contours *RHESSI* sources at different energy intervals, as indicated by the legend on the top right. The contour levels show the 50% and 90% of the maximum intensity of the *RHESSI* images, which are integrated over the interval 15:58:40–15:59:40 UT by using the standard image reconstruction algorithms (see Sect. 5). The *RHESSI* sources show the presence of very energetic electrons (above 100 keV) and coincide with the loop top of the flare, suggesting that we are observing a coronal HXR source. Such a bright coronal source cannot be interpreted in the standard thin-target scenario, but it shows properties similar to some of the coronal hard X-ray sources discussed in (e.g., Krucker et al. 2008, and references therein). Note that there is also a *RHESSI* footpoint source outside the field-of-view of Figure 2, which is detectable above ≈ 30 keV, see Gary et al. (2018). Figure 2 also shows a microwave source observed by *EOVSA* between 15:59:08 UT and 15:59:12 UT. This source is located at and above the HXR looptop source, with a characteristic non-thermal gyrosynchrotron spectral shape and a maximum brightness temperature of over 3×10^9 K, suggesting the presence of highly energetic, mildly relativistic electrons in the loop top region.

The Fe XXIV 255.10 Å line is intense enough in the location of box 1, so that the fitting of the spectra (in particular the line wings) can be reliably performed. This location coincides well with the contours of the *RHESSI* high-energy sources. The line is saturated on the left side of box 1, and too faint on its right side. On the other hand, the Fe XXIV 192.03 Å is saturated where the *RHESSI* sources are most intense, and we can reliably fit the line only in the region indicated by box 2. Although the saturation threshold of EIS is around 1.5×10^4DN, we believe that non-linear effects in the instrumental gain might be important below this value, resulting in an underestimation of the peak for very intense lines. For this reason, we do not analyze line profiles with peak intensities above $\approx10^4$ DN. We also only select profiles where the interpolation algorithm has removed most of the missing pixels, with the exception of maximum 2 pixels.

To fit the Fe XXIV 255.10 Å and 192.03 Å lines, we use either a single (or multi-) Gaussian or a κ fit, this latter performed by using the method described in Section 2.3 of Dudík et al. (2017a). In particular, we perform a convolution of the EIS instrumental Gaussian profile and a κ profile by using a modified version of the SSW `comp_gauss.pro` routine. This convolution has the form (cf., Jeffrey et al. 2016, 2017)

$$I(\lambda) = I_0 \int_{-\infty}^{\infty} \mathrm{e}^{-\frac{(\lambda-\lambda')^2}{2w_{\mathrm{instr}}^2}} \left(1 + \frac{(\lambda'-\lambda_0)^2}{2(\kappa-3/2)w_\kappa^2}\right)^{-\kappa} \mathrm{d}\lambda' \,, \tag{1}$$

where I_0 is the peak intensity, λ_0 is the wavelength of the line center, w_κ is characteristic width, and κ is the non-Maxwellian parameter.

As mentioned in Sect. 2.1, the EIS instrumental width w_{instr} varies between the two Fe XXIV lines and it is estimated to be ≈0.0704 Å and 0.0698 Å for the 192.03 Å and 255.10 Å lines respectively, as calculated using the SSW routine `eis_slit_width.pro`.

For both the Gaussian and κ fits, the weights W are given by:

$$W = \sqrt{\frac{1}{\sigma^2(I(\lambda_i))}} \tag{2}$$

where $\sigma(I(\lambda_i))$ are the intensity errors obtained from `eis_prep.pro`, which take into account the photon statistics noise, pedestal, and the error of the dark current.

To evaluate the goodness-of-fit, we use the reduced χ^2_{red} (e.g., Eq. (18) of Dudík et al. 2017a), as well as the residuals R of the fits, obtained as:

$$R = I_{\mathrm{obs}}(\lambda_i) - I_{\mathrm{fit}}(\lambda_i) \tag{3}$$

where I_{obs} and I_{fit} are the observed spectra and fit respectively for each wavelength λ_i. Note that in the following sections we will mostly express the width of the fitted lines in terms of characteristic widths w_{G} or w_κ as obtained from either the Gaussian or κ fit respectively. In order to convert from w_κ to FWHM$_\kappa$, we use Eq. 14 of Dudík et al. (2017a), which we recall here for the reader's convenience:

$$w_\kappa = \frac{1}{8}\frac{FWHM_\kappa}{(\kappa-3/2)(2^{1/\kappa}-1)} \tag{4}$$

For the Gaussian fit, w_{G} is simply equal to:

$$w_{\mathrm{G}} = \frac{FWHM_{\mathrm{G}}}{\sqrt{8\ln 2}} \tag{5}$$

The fitting procedure for the Fe XXIV 255.10 Å and 192.03 Å lines are discussed separately in Sects. 3.1 and 3.2.

3.1. *Fe XXIV 255 Å line fitting*

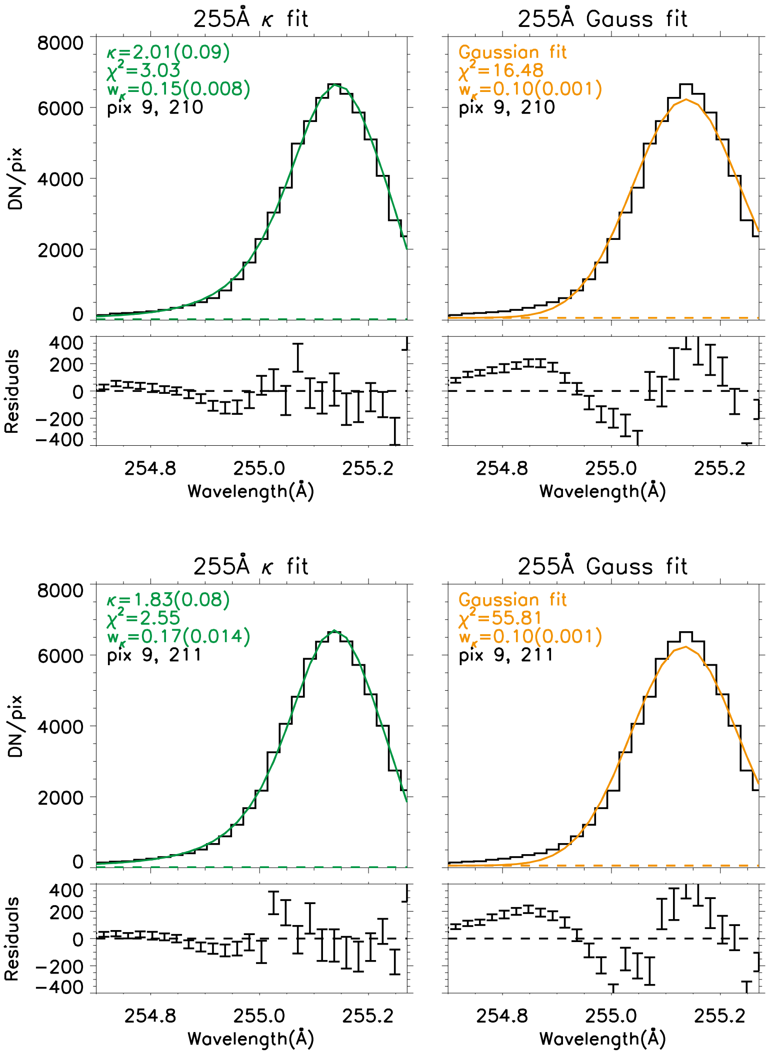

Figure 3. Example of κ (left panels) and single Gaussian (right panels) fits of the EIS Fe XXIV 255.10 Å line during the raster exposure 9 and the slit pixels 210 and 211 (top and bottom panels respectively) inside box 1 of Fig. 2. For each fit, the value of χ^2 is indicated in the left top part of the panel, as well as the width of the line obtained by the fit and its uncertainty. For the κ fit, also the value of κ and associated error are shown. Note that the line width has a different interpretation for a κ and Gaussian fit, see text for more details.

Figure 3 shows two examples of Fe XXIV 255.10 Å spectra at X-pixels = 9 and Y-pixels = 210 and 211 within box 1, which have been fitted with a single κ (left panel) and Gaussian (right panel) function. The results of the fit ($\chi^2_{\rm red}$ value, κ value and line width expressed in Å, with corresponding errors) are indicated in the same panels. At the bottom of both panels, we show the fitting residuals along the spectra (see Eq. 3). We found that in both cases the single κ fit performs much better than the Gaussian one, with considerably lower values of $\chi^2_{\rm red}$ and residuals. The same result is obtained for all the "good" pixels in box 1 ($\approx$10) that we selected according to the criteria described above, as also discussed in Sect. 6. We note that the red wing of the line is partially outside the spectral window, whereas the blue wing can be properly fitted. The fact that part of the spectrum is missing can potentially create some problems in the convolution part of the fitting algorithm. To rule this out, we compared the results of the convolution (Eq. 1) and fit with a purely κ-profile (Dudík et al. 2017a),

$$I(\lambda) = I_0 \left(1 + \frac{(\lambda - \lambda_0)^2}{2(\kappa - 3/2)w_\kappa^2}\right)^{-\kappa} \mathrm{d}\lambda\,, \qquad (6)$$

and verified that there is no significant difference (within the uncertainties) between the κ and line width values estimated using the convolution or purely κ fit. This is not surprising, since the lines are much broader than the EIS instrumental width. As discussed in Dudík et al. (2017a), the pronounced wings can also be reproduced by a combination of two Gaussians profiles, which can be interpreted as the superposition of emission from plasma formed at two different temperatures. To investigate this possibility, we performed a double-Gaussian fit of the Fe XXIV 255.10 Å in the same pixels of box 1. Since the spectrum is missing its red wing, in most cases the uncertainties of the two-component fits were too high (with a $\chi^2_{\rm red}$ value much less than 1), except from one pixel (raster exposure 8, Y-pixel 210). Figure 4 shows the comparison of the κ, Gaussian and double-Gaussian

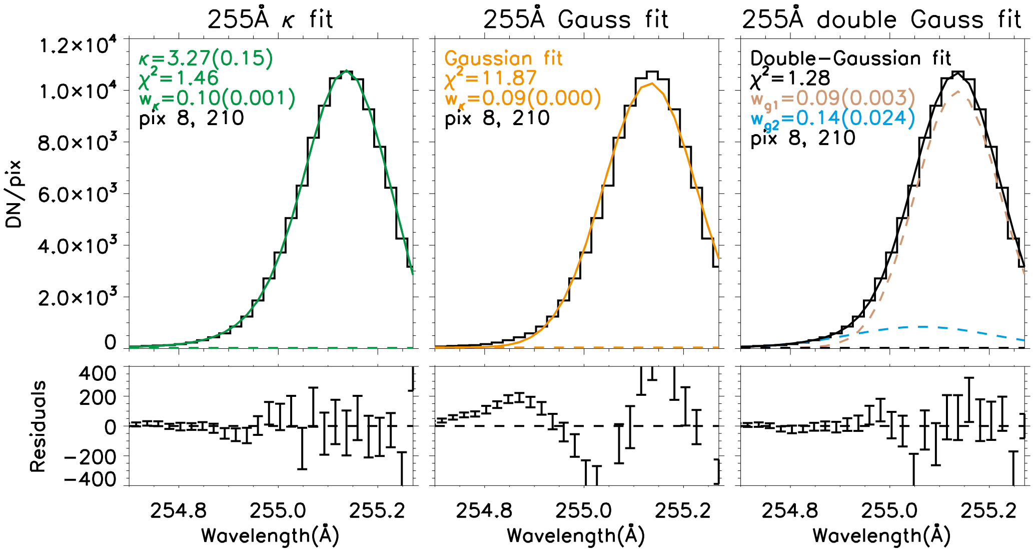

Figure 4. Example of κ (left panel) , single Gaussian (middle panel) and double-Gaussian (right panel) fits for the EIS Fe XXIV 255.10 Å line during the raster exposure (X-pixel) 8 and the slit Y-pixel 210 (box 1 of Fig. 2). See caption of Fig. 3 and text for more details.

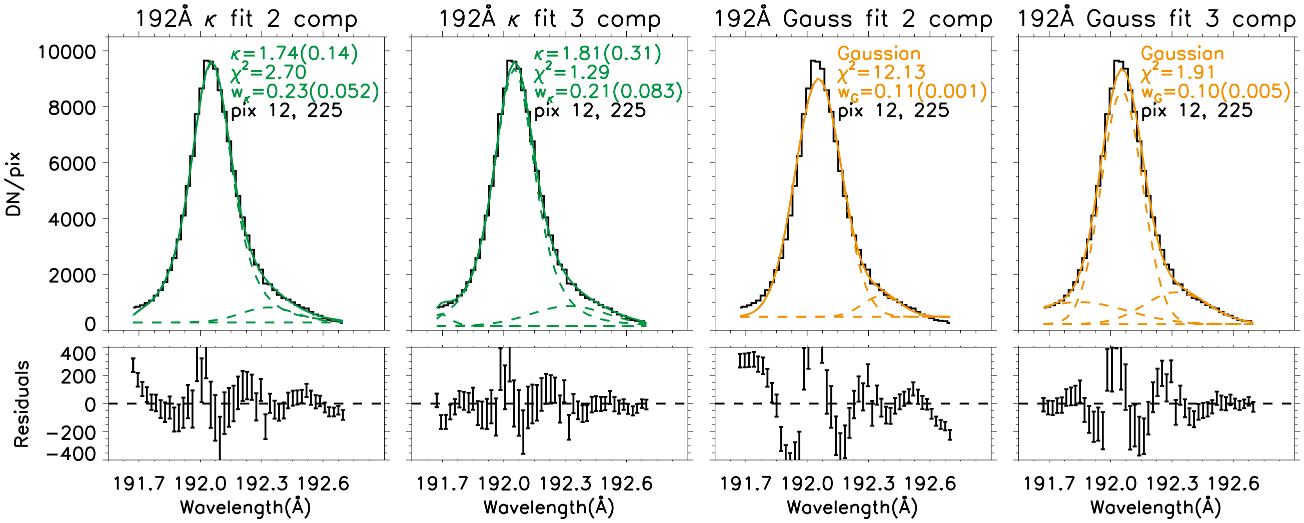

Figure 5. *From left:* Example of κ fit and Gaussian fit with 1 or two blends for the EIS Fe XXIV 192.03 Å line during the raster exposures 12 and the slit pixels 225 (box 2 of Fig. 2). See caption of Fig. 3 for more details on the figure.

fit for this single case. The FWHM obtained from the double-Gaussian fit (using Eq. 5) are of the order of 0.20 and 0.34 Å for the two Gaussian components, which can be used to estimate the required non-thermal velocity as follows:

$$v_{\rm nth} = \frac{c}{\lambda_0} \frac{1}{2\sqrt{ln2}} \sqrt{(w^2 - w_{\rm instr}^2 - w_{\rm th}^2)} \,. \qquad (7)$$

Using the equation above, we can estimate that the line width of the broader Gaussian component corresponds to very large non-thermal velocities (of the order of ≈300 km s^{-1}). Although we cannot completely rule out the possibility of fitting the large wings with two Gaussian components, a single κ fit appears as a possible simple explanation to account for the non-Gaussian shape of the line. Note that the line width obtained from the κ fit (≈ 0.10 Å, see Fig. 4) corresponds to a FWHM$_\kappa$ of 0.19 Å (using Eq. 4) and thus to a lower value of non-thermal velocity (≈150 km s^{-1}).

3.2. *Fe XXIV 192 Å line fitting*

The Fe XXIV 192.03 Å line is the most intense of the observed EIS flare lines, as its centroid is close to the peak of sensitivity of the spectrometer. Unfortunately, the line was saturated in box 1, where the *RHESSI* HXR sources are located. Nevertheless, the line could be reliably observed in the region indicated by box 2 in Fig. 2, which is also located along the plasma sheet feature. In contrast to the Fe XXIV 255.10 Å line, both wings can be observed in the 192.03 Å spectrum. In most

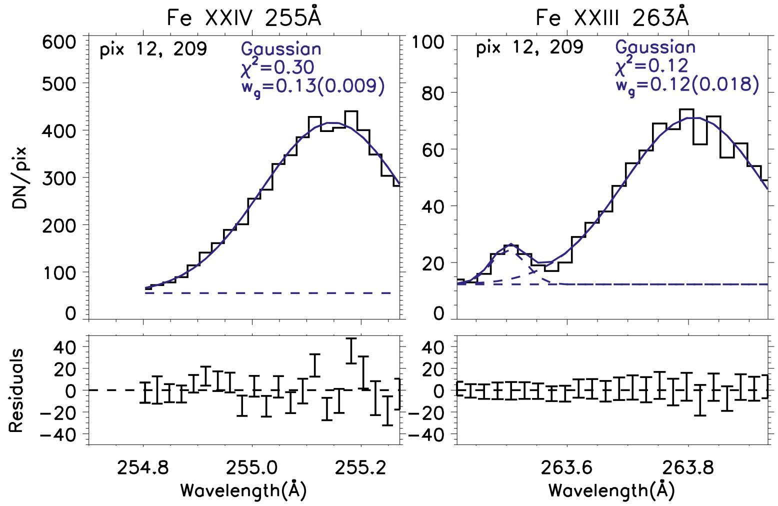

Figure 6. Sample spectra of the Fe XXIV 255.10 Å (left panel) and Fe XXIII 263.76 Å (right panel) lines for raster exposure 12, Y-pixel 209 for the LW detector (corresponding to Y-pixel ≈225 in the SW detector). The spectra show that the lines are quite broad at this location, with $w_{\rm G}$ equal to 0.13±0.009 Å (or $FWHM_{\rm G}$ = 0.030±0.02 Å) for the Fe XXIV 255.10 Å line.

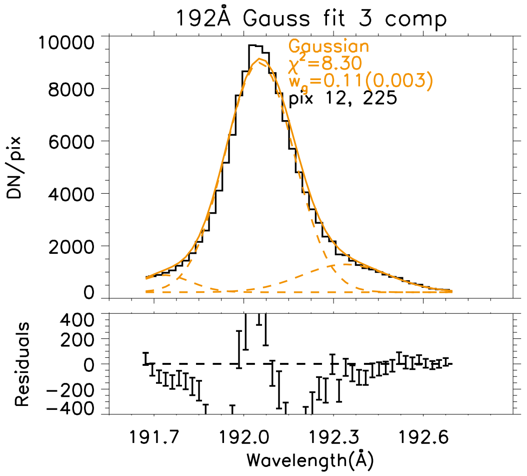

Figure 7. Gaussian fit with two blends for the EIS Fe XXIV 192.03 Å line during the raster exposure 12 and slit Y-pixels 225 (box 2 of Fig. 2), obtained by fixing the minimum value of the line width to $w_{\rm G}$ of around 0.11 Å (or $FWHM_{\rm G}$ 0.026 Å, see text for more details).

pixels of box 2, the line shows the presence of a blend in the red wing and possibly a less intense one in the blue wing. The origin of both these blends is unclear. One may think that the blend on the red wing of the Fe XXIV 192.03 Å line might be due to the Fe XII transition at 192.39 Å. To investigate this possibility, we estimate the predicted intensity of the Fe XII 192.39 Å line by measuring the intensity of another Fe XII transition at 186.88 Å and using the theoretical ratio of these two lines from CHIANTI. We find that the predicted intensity of Fe XII 192.39 Å is significantly lower (by a factor of ≈50) than the intensity of the observed blend on the red side of the Fe XXIV 192.03 Å line, and we can thus rule out this interpretation. Another possible explanation may be that we are observing an unknown transition or a red-shifted component of the Fe XXIV 192.03 Å line. Such redshifted component might not be observed in the Fe XXIV 255.10 Å spectra as in that case the line partially lies outside the spectral window.

Figure 5 shows an example of the Fe XXIV 192.03 Å spectrum at the raster exposure (or X-pixel) 12 and Y-pixel 225, which corresponds to Y-pixels ≈ 208–209 for the Fe XXIV 255.10 Å observation, considering the offset of ≈16.5 pixels between the SW and LW channels. The four panels of Fig. 5 show the results of different fitting procedures that we applied to the same spectrum (from left to right): a κ fit with the one or two blends and a Gaussian fit with one or two blends. It should be noted that the blends in the κ fit are assumed to be Gaussian, because their intensity lines is too low to determine the shape of their profiles, as well as to limit the number of free parameters of the fit. Figure 5 shows that a κ distribution plus only one blend on the red wing of the line provides a very good fit of the observed spectrum, without the need of adding an extra component on the blue side of the Fe XXIV line. This is not the case for the Gaussian fit, where two extra components are required. These components also need to be very large to properly fit the line profile, resulting in a width for the Fe XXIV line which is narrower that the ones observed for the Fe XXIV 255.10 Å and Fe XXIII 263.76 Å lines, as shown in Fig. 6. While these two latter lines are too faint to perform a reliable fit of their wings (see the $\chi^2_{\rm red}$ value well below 1), their $FWHM_{\rm G}$ values are estimated from the Gaussian fit to be around 0.30 Å for the Fe XXIV 255.10 Å line and 0.27 Å for the lower temperature Fe XXIII 263.76 Å line (corresponding to $w_{\rm G} = 0.13$ Å and 0.12 Å respectively), as indicated in Fig. 6. It is reasonable to assume that the width of the Fe XXIV 192.03 Å would be at least as large as the width of the other Fe XXIV line. However, if we fix the minimum $FWHM_{\rm G}$ of the Fe XXIV 192.03 Å line to be at least equal to a conservative value of 0.26 Å (or equivalently $w_{\rm G}$ = 0.11 Å) in the 3 component Gaussian fit, this latter does not perform as well, with a value of $\chi^2_{\rm red}$ and residuals which are significantly larger than those obtained for the 3 component κ fit (see

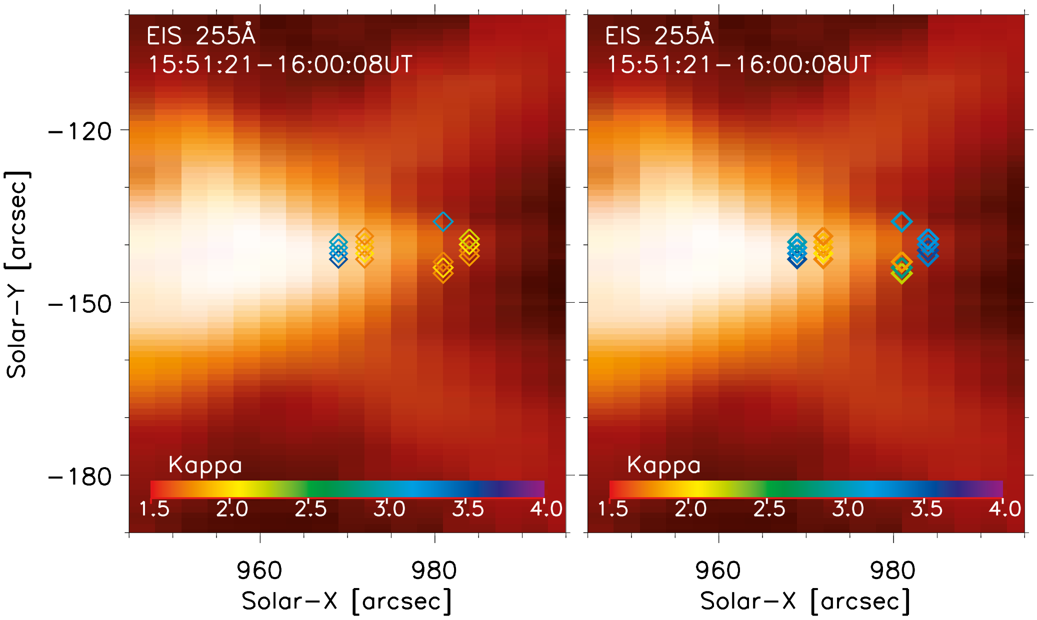

Figure 8. Distribution of κ values obtained by fitting the Fe XXIV 255.10 Å and Fe XXIV 192.03 Å lines overlaid on intensity images formed in the EIS Fe XXIV 255 Å line . The fit of the Fe XXIV 192.03 Å line includes 1 or 2 blends (left and right panels respectively).

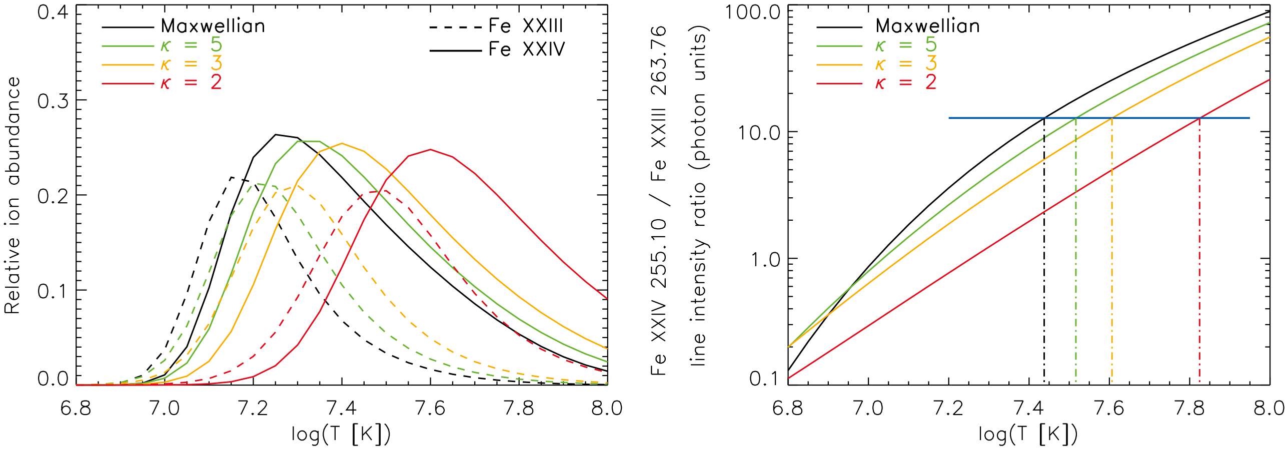

Figure 9. *Left panel*: fractional ion abundance for Fe XXIII and Fe XXIV for a Maxwellian distribution (black line) and non-Maxwellian distributions with different values of κ, as indicated in the legend. *Right panel*: Theoretical Fe XXIV 255.10/Fe XXIII 263.76 Å ratio for electron Maxwellian (black line) and non-Maxwellian distributions with different values of κ, as indicated in the legend. The horizontal line indicates the observed ratio of 12.8 in box 1.

Fig. 7). We consider this an additional indication that the Fe XXIV 192.03 Å line, even if blended, is best fitted with a κ rather than a Gaussian profile.

The κ values obtained from fitting the Fe XXIV 192.03 Å and 255.10 Å lines are summarized in Fig. 8, assuming two (i.e. one line blend, left panel) or three components (i.e. two line blends, right panel) for the fit of the 192.03 Å line.

4. TEMPERATURE DIAGNOSTICS BASED ON THE Fe XXIV 255.10/Fe XXIII 263.76 Å RATIO

We use the ratio of the Fe XXIV 255.10 Å and Fe XXIII 263.76 Å lines to estimate the *electron* temperature T_e of the emitting plasma in the location indicated by box 1 in Fig. 2 at around 15:59 UT. We convert the Fe XXIV and Fe XXIII intensities from DN to physical units (i.e. phot s^{-1} cm^{-2} $arcsec^{-1}$) using the radiometric calibration of Del Zanna (2013). As mentioned in Sect. 2.1, the EIS radiometric calibration may need to be revised to take into account of the instrument degradation after 2014. Nevertheless, problems in the calibration should not affect our results dramatically as we use lines which are close in wavelength and are included in the same CCD detector. We find that the ratio estimated using the radiometric calibration from Del Zanna (2013) (≈12.1) is very similar to the one obtained using the ground calibration (≈12.8). This is not surprising as the correction factor shown in Del Zanna (2013) appears to be similar in the wavelength interval around 250–260 Å (see middle panel of Fig. 8 of Del Zanna

2013). We note that the in-flight calibration produces only a difference of ≈0.02 in the resulting $\log(T\,[\mathrm{K}])$ estimated from the Fe XXIV 255.1 Å / Fe XXIII 263.8 Å line intensity ratio. A ratio of 12.1 indicates a temperature of $\log(T\,[\mathrm{K}])$ 7.44 in the Maxwellian case (see the right panel of Fig. 9).

We also investigated the effect of taking into account non-Maxwellian conditions in the local plasma on the temperature diagnostic. Figure 9 (left panel) shows the fractional ion abundance of the Fe XXIII and Fe XXIV lines for the Maxwellian and κ-distributions with different values of κ, as obtained using the KAPPA package (Dzifčáková et al. 2015) and CHIANTI v8. We note that these ionization equilibria were obtained by assuming *electron* κ-distributions, which may not necessarily be the same as *ion* distributions (see Sect. 7.1 of Dudík et al. 2017a, as well as our Sect. 6). We note that the peak formation temperature of the Fe XXIII and Fe XXIV lines is strongly shifted to higher values for decreasing values of κ. In turn, the calculated Fe XXIV 255.10/Fe XXIII 263.76 Å ratios as a function of different κ, shown in the right panel of Fig. 9, are also shifted to higher T_e (c.f., Dzifčáková et al. 2018). The horizontal blue line in this panel indicates the observed ratio in box 1. Fig. 9 shows that the temperature diagnostic varies significantly with κ, from $\log(T_\mathrm{e}\,[\mathrm{K}]) \approx$ 7.44 for Maxwellian to 7.82 for $\kappa = 2$, see dot-dashed lines in the right panel of Fig. 9. In particular, using the average value of κ obtained from the fit of the Fe XXIV 255.10 Å spectra in box 1 (≈2–3 see Sect. 3.1 and Fig. 8), we estimate a temperature of the hot plasma at the plasma sheet feature of the X-class September 10 2017 flare to be between $\log(T_\mathrm{e}\,[\mathrm{K}]) = 7.6$ and 7.8. This value is significantly higher than the corresponding Maxwellian one (see also Warren et al. 2018, Figures 5–6 therein), by a factor of ≈2.4 for $\kappa = 2$. These results are in line with the non-Maxwellian temperature diagnostics of Dzifčáková et al. (2018).

We also note that the diagnosed temperatures are above the corresponding ionization peaks of Fe XXIV independently of whether the conditions are Maxwellian or non-Maxwellian. Such high temperatures have been reported before (Tanaka et al. 1982) and in the context of our observation, they suggest that the the presence of cool line blends (such as Fe XVII, e.g. Del Zanna 2008) on the wings of the Fe XXIV lines is unlikely, justifying the fitting procedures as described in Sect. 3.

Using the temperature diagnostic obtained by the Fe XXIV and Fe XXIII line ratio in box 1, we can also provide a rough estimate of the electron number density N_e in the plasma by using the emission measure (EM_h) obtained from the AIA images in the 193 Å filter:

$$EM_h = \frac{I_\mathrm{obs}}{R_{193\,\mathrm{\AA}}(T)} \qquad (8)$$

where I_obs is the observed averaged intensity of the AIA 193 Å image in box 1 at 15:59 UT, expressed in DN s^{-1}. $R_{193\,\mathrm{\AA}}(T)$ is the AIA response function in the 193 Å filter, which can be obtained by using the effective area provided by the SSW routine `aia_get_response.pro`, atomic data from CHIANTI v8 (Dere et al. 1997; Del Zanna et al. 2015) and photospheric abundances from Asplund et al. (2009), following the method described in the appendix of Del Zanna et al. (2011). Assuming the range of temperatures ($\log(T\,[\mathrm{K}]) \approx 7.3$–7.7) obtained from the Fe XXIV 255.10/Fe XXIII 263.76 Å ratio for Maxwellian and κ distributions, we obtain EM_h values varying between 5.2×10^{31} cm^{-5} and 1.8×10^{32} cm^{-5}.

The plasma density can thus be estimated by using the following formula:

$$N_\mathrm{e} \approx \sqrt{\frac{EM_\mathrm{h}}{N_\mathrm{H} \times N_\mathrm{e} \times h}} \qquad (9)$$

where h is depth of the plasma sheet, estimated by Warren et al. (2018) to be ≈$10^{8.9}$ cm. The hydrogen density N_H can be expressed as 0.83 N_e in a fully ionized gas with helium abundance relative to hydrogen A(He) = 0.1. Using Eq. 9 and the values of EM_h above, we obtain densities of the order of 2.8–5.3 10^{11} cm^{-3} in the plasma sheet (at the location indicated by box 1 in Fig. 2) during the impulsive phase of the September 10 2017 flare. These densities can be directly compared with the values obtained from the analysis of the *RHESSI* spectra, as will be described in Sect. 5.

5. ANALYSIS OF *RHESSI* DATA

RHESSI (Lin et al. 2002) started detecting the flare at ≈ 15:53 UT, while the very beginning of the flare was missed by the instrument, which was in the night part of its orbit. During the impulsive phase until ≈ 16:00 UT, the lightcurves of the HXR emission show several bursts up to ∼ 300 keV, whereas the emission at energies below ∼ 25 keV rises smoothly. We analyzed *RHESSI* spectra and images observed around 15:59 UT, when the EIS slit passed over the *RHESSI* HXR source. Despite the thick attenuator, i.e. the A3 state, was in place at that time, the *RHESSI* data are still affected by pile-up effects which distort the spectra formed in the ≈ 30 − 50 keV range. Currently, the pile-up cannot be corrected for when reconstructing the *RHESSI* images. Therefore, in Fig. 2 the 30–50 keV energy range is omitted and the *RHESSI* sources are shown at energies below and above it. Figure 2 shows that the *RHESSI* sources are cospatial with the upper parts of the bright loops as seen e.g. in the AIA 193 Å filter.

The *RHESSI* spectra were analyzed individually for for detectors 3 and 8 (which seem to be less affected by pile-up than detectors 1 and 6) and fitted within the 12 − 250 keV energy range. Energies below 12 keV were not included in the spectral analysis due to unknown instrumental effect modifying spectra in the A3 state. In order to take into account the pile-up effects for the spectral analysis, `pileup_mod` fitting function was used. We analyzed the *RHESSI* spectrum accumulated during the time interval 15:59:04-15:59:16 UT, corresponding to the EIS box 1, in Fig. 2.

The fits have revealed that a multi- or a double-thermal component dominating emission up to ∼ 50 keV is needed to describe the *RHESSI* spectrum well. Both models are similar in terms of χ^2 and residuals. Fitting with a multi-thermal component, assuming that differential emission measure has a power-law dependence on temperature ($\sim T^{-\alpha}$), results in: a power-law index $\alpha \approx 6.3$, differential emission measure at $T = 23$ MK

(2 keV) $DEM_{23} = 15 \times 10^{49}\,\mathrm{cm}^{-3}\,\mathrm{kev}^{-1}$, and a maximum temperature $T_{\mathrm{m}} = 55{-}92$ MK. On the other hand, the fit using a double-thermal component reveals the presence of a super-hot component, $T_{\mathrm{sh}} = 43{-}56$ MK, which dominates the HXR spectra in $\sim 18-30$ keV energy range, see Fig. 11. The *RHESSI* source reconstructed at this energy range is shifted towards higher coronal heights compared to the thermal source, $T = 21$ MK at lower energies $9{-}12$ keV (see Fig. 10), similarly as the super-hot sources reported by Caspi & Lin (2010); Caspi et al. (2015). The separation between thermal and super-hot sources is rather small, around 1-2$''$, but is seen consistently in all three different algorithms used for the image reconstruction (MEM NJIT, UV_Smooth, and VIS FWDFIT). Although source sizes and positions slightly differ between algorithms, the reconstructed *RHESSI* sources are similar in terms of modeled and observed modulation profiles and visibilities. We estimated a source area S and volume V from the 50% intensity contour of the reconstructed images, taking $V = 4/3\pi(S/\pi)^{3/2}$. Then, using the fitted emission measure of the thermal and super-hot components, $EM = (35-46) \times 10^{49}\,\mathrm{cm}^{-3}$ and $EM_{\mathrm{sh}} = (0.28-0.76) \times 10^{49}\,\mathrm{cm}^{-3}$, and their volume, the electrons density can be determined. The density of the thermal source is high, $N_{\mathrm{e}} = (4.3-13) \times 10^{11}\,\mathrm{cm}^{-3}$, whereas the density of the super-hot source is $N_{\mathrm{e,sh}} = (0.86-2.2) \times 10^{11}\,\mathrm{cm}^{-3}$, again similarly as the one reported by Caspi & Lin (2010) for the 2002 July 23 X4.8 flare. These densities are consistent with the values ($\approx 2.8-5.3\,10^{11}\,\mathrm{cm}^{-3}$) obtained in Sect.4, using the estimated emission measure in the AIA 193 Å channel and temperature diagnostics from the EIS line ratio. Such a high density source can be viewed as an example of a coronal thick-target source type discovered by Veronig & Brown (2004). Assuming source half-length $L = \sqrt{S/\pi}$ and the relation for the beam stopping energy $E_{\mathrm{stop}} \approx \sqrt{10^{-17}nL}$ (e.g. Krucker & Lin 2008), the thermal source region is capable of collisional stopping of electrons of energies up to about $57-72$ keV. Indeed, the *RHESSI* loop-top source in the $50-100$ keV range overlaps with the *RHESSI* thermal source and has a comparable size. However, we note that a *RHESSI* footpoint source in energies above 30 keV does exist Gary et al. (2018). This could suggest that the footpoint source might not not in the same loop/magnetic field as the loop-top source.

Given the nature of *RHESSI* sources, a thick-target component at energies above $\sim$ 50 keV was used in spectral analysis of spatially integrated *RHESSI* spectra. The observed *RHESSI* spectrum can be fitted with an injected electron power-law beam of $\delta \approx 4$, which is significantly harder than the values reported by Veronig & Brown (2004). Although the *RHESSI* source in the $100-300$ keV range overlaps with the thermal source, it has a more elongated shape and cannot be interpreted as a thick-target region for electrons of such energies. Using the half-length measured across the 50% intensity contour, the stopping energy is in the $77-130$ keV range. Therefore, it is also relevant to use the thin-target approximation. Figure 11 shows such an example for a thin-target kappa distribution (see Kašparová & Karlický 2009; Oka et al. 2013). Further, the spectra can be fitted with a thin-target power-law beam equally well in terms of χ^2 and residuals. While the power-law index thus obtained is ≈ 2.5, κ ranges between 2.1 and 2.4. These values are consistent to the ones derived for ions from the EIS line fitting (Sect.3).

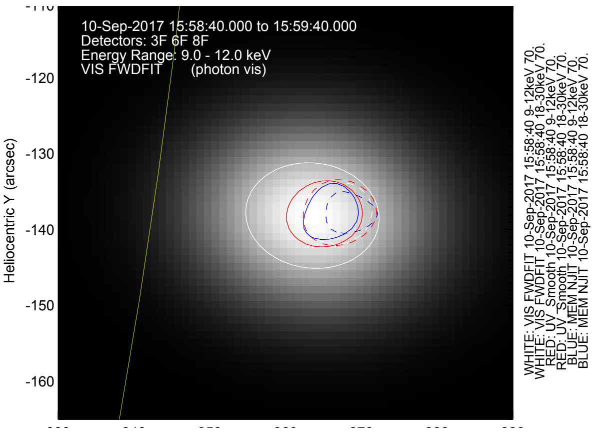

Figure 10. *RHESSI* sources in the $9-12$ keV (full lines) and $18-30$ keV (dashed lines) range reconstructed by three image algorithms: VIS FWDFIT (white), UV_Smooth (red), and MEM NJIT (blue). The background image is VIS FWDFIT image in the $9-12$ keV range. Countours are displayed at the 70% intensity level.

Note that at energies below 50 keV the *RHESSI* spectrum can be fitted by a single kappa distribution instead of two thermal components. Although such a component has fewer free parameters, due to the different source sizes and positions in the energy ranges $9-12$ keV and $18-30$ keV where each of the thermal components dominates, we excluded such a fitting function as inappropriate. Finally, the *RHESSI* spectrum cannot be fitted well enough with two components only, e.g. with a thermal component and a beam single power-law/κ component (as in Oka et al. 2015). A reasonable fit can also be obtained for a double power-law beam with a steep (soft) spectrum above $\sim$70 keV only, i.e. mimicking the nature of a multi- or double-thermal component. Such a fit was not interpreted as more appropriate.

6. DISCUSSION AND INTERPRETATION

We now proceed to discuss the possible interpretation of the observed line profiles and *RHESSI* spectra.

Jeffrey et al. (2016) listed three possible interpretations to the observed κ emission line profiles in solar flares:

1. Plasma is multithermal along the line of sight;
2. Fe ions are accelerated isotropically to a non-Maxwellian distribution of velocities;
3. Turbulence is present, in terms of macroscopic parameters (T, n_{e}, or velocities).

We shall deal with these in the following subsections.

6.1. *Multithermal plasmas*

The interpretation (1) is based on the fact that any non-Maxwellian distribution with a thermal core and a tail can be represented by a linear combination of Maxwellians with different temperatures. For a κ-distribution, this Maxwellian decomposition and its coefficients was provided by Hahn & Savin (2015). In terms

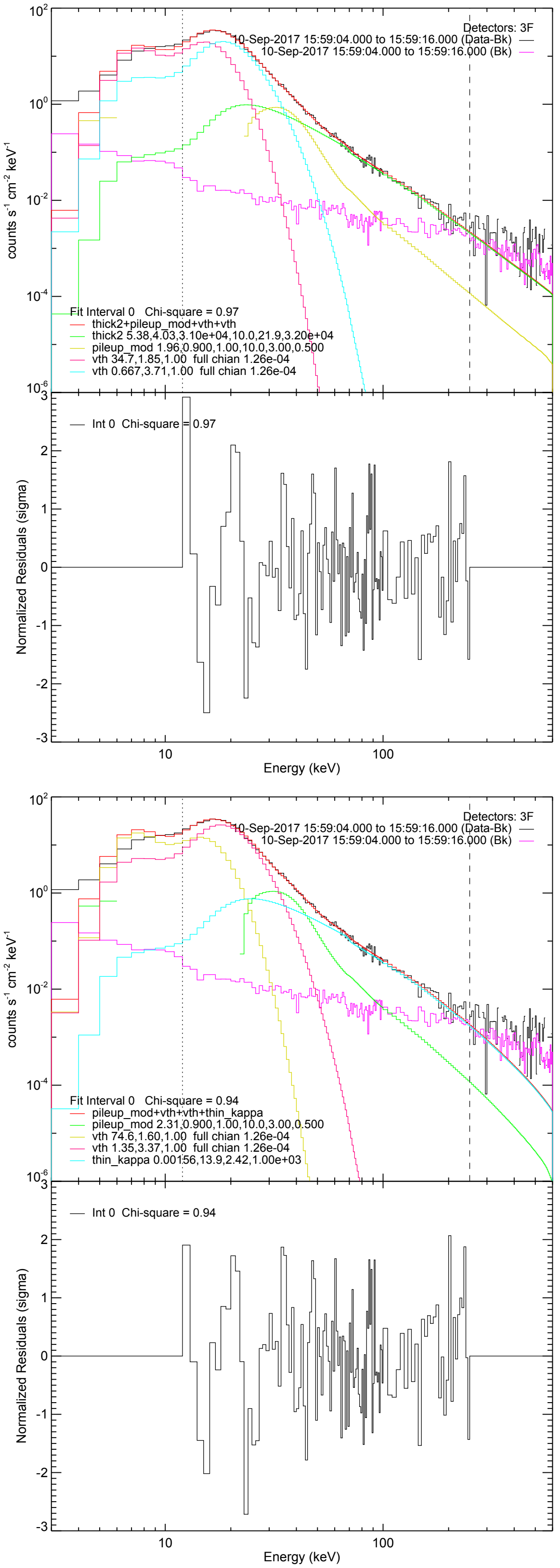

Figure 11. *RHESSI* spectra of 3F detector: Left: Forward-fitted spectrum using two thermal components, vth, a correction for pile-up effects, pileup_mod, and a thick-target power-law beam, thick2. Residua of the modelled and observed spectra are showed below the spectrum. Right: The same as in the left panel but using a kappa distribution in the thin-target approximation, thin_kappa, instead of the thick-target beam component.

of the line profile fitting, one should fit a series of Gaussians to the line profile, each representing a Maxwellian at a given temperature. We have seen in Sect. 3.1 that such fitting is unconstrained, with the exception shown in the right panel of Figure 4. Using the widths of such double-Gaussian fit, $w_{\mathrm{G}1,2}$, we obtain equivalent ion temperatures $T_{\mathrm{G}1,2}$ (also called Doppler temperatures) by using the formula (compare Eqs. (8) and (10) of Dudík et al. 2017a):

$$w_{\mathrm{G}}^2 - w_{\mathrm{instr}}^2 = \frac{k_{\mathrm{B}} T_{\mathrm{G}}}{m_{\mathrm{Fe}}} \frac{\lambda_0^2}{c^2}\,, \tag{10}$$

where we subtracted the w_{instr}^2 factor to account for the instrumental broadening. Eq. (10) yields yields $T_{\mathrm{G}1,2} = 62$ and 99 MK for the two Gaussians, respectively. Both are significantly higher (by factors of $\approx$2.3 and 3.6) than the corresponding T_{e} derived from the Fe XXIV / Fe XXIII line intensity ratio (Sect. 4). If the plasma were really multithermal with dominant temperature components at $T_{\mathrm{G}1}$ and $T_{\mathrm{G}2}$ (assuming equilibrium between electrons and ions), the T_{e} obtained should be correspondingly higher. Since it is not, we suggest that the multithermal interpretation is not likely.

6.2. *Accelerated ions*

The interpretation (2), namely that ions are accelerated, is in line with recent theoretical modeling of Li et al. (2017), who showed that ions can be accelerated preferentially to electrons in flare conditions. That the ion profiles could be due to accelerated ions has also been thoroughly examined by Jeffrey et al. (2017), who used the formulae derived by and adapted from Sigmar & Joyce (1971) and Stix (1972) to calculate the thermalization time for accelerated ions; in their case, Fe XVI and Fe XXIII. The thermalization timescale τ_f was derived to be $\approx 10^{-2}$ s. In our case, using the values of $N_{\mathrm{e}} = 5 \times 10^{11}$ cm^{-3} and T_{e} derived in Sect. 4, the corresponding ion thermalization timescales would be even shorter by about 2 orders of magnitude.

However, we note that the formula (13) of Jeffrey et al. (2017) is applicable only for ion velocities v satisfying $v_{\mathrm{th,i}} \ll v \ll v_{\mathrm{th,e}}$, where v_{th} are ion and electron thermal speeds, equal to $\sqrt{2 k_{\mathrm{B}} T_{\mathrm{e,i}} / m_{\mathrm{e,i}}}$, respectively. In our case, the condition $v_{\mathrm{th,i}} \ll v$ is broken: If we suppose that the ions are accelerated to a κ-distribution corresponding to $\kappa \approx 2$ profiles shown in Figures 3, we obtain, as an order-of-magnitude estimate, Doppler velocities $v \approx 300$ km s^{-1} for the far wings of the Fe XXIV 255.1 Å line at $\Delta\lambda \approx 0.25$ Å, since $\Delta\lambda / \lambda_0 = v/c$. If we assume that the ions have the same temperature as electrons, i.e., $\log(T_{\mathrm{e}}$ [K]$) = 7.4$–7.8 derived in Sect. 4, we obtain ion thermal velocities of 90–140 km s^{-1}; i.e., of the same order-of-magnitude. Thus, the formula (13) of Jeffrey et al. (2017) for calculation of ion thermalization timescales may not be entirely applicable in our case.

Jeffrey et al. (2017) invoked the results of Bian et al. (2014) to conclude that if the line profiles are due to accelerated ions, then the ions must be accelerated locally and continously during the flare. This conclusion is based on the fact that, according to Bian et al. (2014), the κ^* index (with $\kappa^* = \kappa + 1$, Livadiotis & McComas 2009, see Sects. 3 and 4.1 therein) is a parameter describing the ratio of the competing acceleration and collisional timescales, $\kappa^* = \tau_{\mathrm{acc}}/2\tau_{\mathrm{coll}}$. Such conclusion is natural, since the short ion thermalization timescales mean that if the acceleration process is turned off, the ions thermalize much faster compared to EIS exposure times; therefore, if non-Gaussian lines are observed, the acceleration process must persist.

If our line profiles are also due to accelerated ions, then the conclusion of Jeffrey et al. (2017) is again valid and straightened both in terms of acceleration being local as well as continuous. This is because in our case, the ion thermalization timescales are even shorter, while we get similar values of κ^*. Since the thermalization timescale is proportional to τ_{coll}, and $\tau_{\mathrm{coll}} = \tau_{\mathrm{acc}}/2\kappa^*$, and since the thermalization length $L_f = v\tau_f$ is proportional to the product of ion velocity and thermalization timescale, our smaller thermalization timescale (compared to Jeffrey et al. 2017) means both shorter acceleration timescales and shorter thermalization lengths.

We also emphasize that similar κ values were found for the ion (from the EIS Fe XXIV line profiles) as well as electron (from *RHESSI*) distributions. This consistency suggests that the ions were accelerated and that the acceleration process produced both fast electrons and ions with similar distribution functions.

To summarize, the interpretation that ions are accelerated locally and continuously during the flare, remains a valid candidate for our observation.

6.3. *Turbulence*

Macroscopic turbulence is often invoked as an explanation for the non-thermal line widths, i.e., widths larger than the corresponding thermal ones given by Eq. (10). The reasons for the invocation of turbulence in flare observations are well described e.g. in Sect. 3 of the review of Antonucci (1989). One typical example is given by the observation of large non-thermal widths in the spectra of blueshifted high temperature lines during chromospheric evaporation, which are often explained in terms of turbulent mass motions, or alternatively superposition of unresolved flows (e.g. Milligan 2011; Polito et al. 2015).

Rather than chromospheric evaporation, the non-thermal broadening could also be related to HXR emission during flares, as the onset of non-thermal broadening occurs simultaneously with detection of low-intensity HXR emission, and can even precede the strong HXR bursts (Antonucci 1989, e.g.). Alternatively, the non-thermal broadening could be associated to redshifts (due to small bulk downflows), as reported by Jeffrey et al. (2017), which could drive turbulence. In our case, it is difficult to establish the presence of true donwflows along the flaring structures due to the off-limb geometry, and the uncertainty of the EIS wavelength calibration (Kamio et al. 2010).

The observed consistency of non-thermal broadenings observed in lines of ions of different elements and (e.g. Doschek et al. 1979, Table 1 therein), and the absence of variation with the flare position on disk or limb (in contrast to what expected by assuming that the broadening is caused by superposition of flows) was also used as an argument in favor of turbulent (random) motions. Further, in these early studies, large differences between equivalent ion temperatures and electron temperatures derived from line ratios were observed for several minutes (e.g. Antonucci 1989), suggesting that the broadening could not be caused by an effective ion-electron temperature difference, as this could not be maintained for such a long timescale.

But is this line of reasoning valid in our case? To test this, we first estimate the equivalent ion temperatures for the ion κ-distributions corresponding to the observed line profiles. We take the value of $w_\kappa = 0.15$ Å for the Fe XXIV line at 255.1 Å from Fig. 3 and calculate the equivalent T_κ using the formula (compare Eqs. (6) and (11)) of Dudík et al. (2017a):

$$w_\kappa^2 = \frac{k_{\mathrm{B}} T_\kappa}{m_{\mathrm{Fe}}} \frac{\lambda_0^2}{c^2} \,. \qquad (11)$$

Note that the w_κ and w_{G} were derived to have the same physical meaning as if interpreted in terms of the equivalent ion temperature. This stems from the temperature having the same physical meaning for a Maxwellian and a κ-distribution. We also note that, unlike for w_{G} (Eq. 10), the instrumental width is already accounted for since the fit is a convolution (see Eq. 1). Using the above formula, we obtain $T_\kappa = 205 \pm 22$ MK, or $\log(T_\kappa\,[\mathrm{K}]) \approx 8.3$. Similarly, for the lowest value of $w_\kappa = 0.10$ (Fig. 4), we would still obtain $T_\kappa = 99 \pm 3$ MK. The uncertainties in these temperatures are calculated using the corresponding uncertainties of w_κ.

An estimate of the upper limit on the uncertainty of T_{e} derived from the Fe XXIV /Fe XXIII line intensity ratio can be obtained by assuming that both the Fe XXIV 255.1 Å and Fe XXIII 263.8 Å line intensities contain not only the photon noise uncertainty, but also the ≈20% calibration uncertainty (Culhane et al. 2007) as well, despite these lines being both observed in the long-wavelength channel of EIS. Doing so would yield electron temperatures of 27 ± 4 MK assuming Maxwellian, 39 ± 7 MK for $\kappa = 3$, and 66 ± 10 MK for $\kappa = 2$, respectively. We emphasize that in general assuming that the ions are formed under non-Maxwellian conditions results in a higher formation temperature (and thus broader thermal widths) than expected in Maxwellian conditions. In turn, this decreases the amount of non-thermal width that needs to be invoked to explain the observed profiles. Nevertheless, the temperatures listed above are still too low compared to the equivalent ion temperatures which are required to explain the observed large widths in this work. The conclusion is thus that turbulence is still a possible explanation for the observed line widths w_κ as well as the non-Gaussian κ profiles. We note that if the turbulent diffusion coefficient is inversely proportional to velocity, a κ-distribution is formed (Bian et al. 2014).

Thus, we estimate the "non-thermal" widths w_{nth} for the non-Gaussian profiles. To a first approximation, this can be done by setting (c.f., Dudík et al. 2017a)

$$w_{\mathrm{nth}}^2 = w_\kappa^2 - w_{\mathrm{th}}^2 \,. \qquad (12)$$

This equation is not exact; rather, it gives a lower limit of the w_{nth}. This is since a convolution of two κ-distributions with the same κ but different w_{th} and w_{nth} is *not* a κ-distribution of the same κ. This arises from the fact that a sum is present in the $(1 + (\lambda - \lambda_0)^2/2\kappa w^2)^{-\kappa}$ sub-integral functions. However, the resulting convolution is slightly wider, but not too different from those obtained using the approximation (12).

For the fit results from Fig. 4, i.e., $\kappa \approx 3$, $w_\kappa = 0.10$, we obtain for $T = 39$ MK that $w_{\rm th} = 0.065$ Å, from which subsequently $w_{\rm nth} = 0.076$ Å (or ≈126 km s^{-1}), a factor of almost ≈1.2 larger than $w_{\rm th}$. Similarly, for the fit results of Fig. 3, i.e., $\kappa \approx 2$, $w_\kappa = 0.15$, we obtain for $T = 66$ MK that $w_{\rm th} = 0.085$ Å, from which subsequently $w_{\rm nth} = 0.124$ Å (or ≈205 km s^{-1}), again a factor of almost ≈1.5 larger than the corresponding $w_{\rm th}$.

We note that the non-thermal velocity of 205 km s^{-1} is among the largest reported in flares, being even higher than the value of ≈160 km s^{-1} reported from X-ray and EUV spectra (e.g., Doschek et al. 1979, 1980; Feldman et al. 1980; Antonucci et al. 1982; Antonucci 1989; Landi et al. 2003; Del Zanna 2008). To our knowledge, there are not many reports of higher non-thermal velocities. For example, Tanaka et al. (1982, Figure 3 therein) reported such velocities from Fe XXVI spectra (but not Fe XXV), decreasing from 250 km s^{-1} during the course of their flare. Antonucci et al. (1986) reported velocities of 220 km s^{-1}. At present, similar non-thermal line widths were seen with EIS in the Fe XXIII line previously by Lee et al. (2017), see their Fig. 9.

6.4. *Super-hot ions due to collisions with high-energy electrons?*

Finally, we turn our attention to a possible explanation not considered by Jeffrey et al. (2016, 2017), which is that the κ distributions might be caused by collisions of super-hot ions with high-energy electrons. This scenario is suggested by the fact that the high-energy tail in the *RHESSI* spectra could be fitted with a κ-distribution with κ values of 2.1–2.4 (Sect. 5), which are similar to the ones obtained from some line profiles (see, e.g., Fig. 3 and 8). Although the fitting of the high-energy tail observed by *RHESSI* yields a well-constrained κ, the corresponding temperatures are not well-constrained. This is due to the fact that the quasi-thermal core of such κ-distribution occurs at low energies, of about ≈20–30 keV (cyan line in the top right panel of Fig. 11), where the spectrum is dominated by the thermal components and pileup. We determined that electron temperatures of about 20–160 MK are still compatible with the observed high-energy tail, without an appreciable change in the χ^2 and residuals of the *RHESSI* spectrum fit. In fact, the top right panel of Fig. 11 shows a fit using a temperature of 14 keV, equivalent to about 160 MK. These temperatures are comparable, at least to within an order of magnitude, to the equivalent ion temperatures T_κ derived in Sect. 6.3.

Could such temperatures be realistic? In the 2D particle-in-cell simulation of Karlický & Bárta (2011), electron temperatures of 60–120 MK are reached during merging of plasmoids occurring due to tearing instability in the current sheet. In addition, the velocity distribution could show high-energy tails, although details depend on the location (see Fig. 6 in Karlický & Bárta 2011). Such process could possibly occur within our flare, and we note that the location of the observed non-Gaussian lines (Figure 8), i.e., the top of the flare arcade as well as in the plasma sheet feature, would both be appropriate with respect to the geometry of Karlický & Bárta (2011), as plasmoids can also impact the top of the flare arcade and merge with it (see also, e.g., Jelínek et al. 2017).

For the above reasons, as well as the fact that the *RHESSI* thermal coronal source is thick-target for energies $\lesssim$57–72 keV (Sect. 5), we proceed to speculate whether the high equivalent ion temperatures could be due to impact of these high-energy $\kappa = 2$ electrons. We first calculate the electron thermalization time due to collisions with both electrons and ions, using Eq. (3.50) of Goedbloed & Poedts (2004)

$$\tau_{\rm e} \approx \frac{1.09 \times 10^{10}}{\ln\Lambda} \frac{\widetilde{T}_{\rm e}^{\,3/2}}{Z_f N_{\rm e}}\,, \tag{13}$$

with $T_{\rm e}$ = 3 keV (≈ 35 MK) and $N_{\rm e}$ = 5 10^{11} cm^{-3}. where $\ln\Lambda \approx 10$ is the Coulomb logarithm, $\widetilde{T}_{\rm e}$ is electron temperature in keV, $N_{\rm e}$ is electron number density in cm^{-3}, and Z_f is the charge of ions involved, which we take $Z_f = 1$. Note that the $\tau_{\rm e}$ scales with $\widetilde{T}_{\rm e}^{\,3/2}$ due to the fact that progressively higher-energy electrons are less collisional. Considering now that the background plasma impacted by the beam has $\widetilde{T}_{\rm e} = 3$ keV ($T_{\rm e} =$ and $N_{\rm e} \approx 5 \times 10^{11}$ cm^{-3}, we obtain $\tau_{\rm e} = 8 \times 10^{-3}$ s. The corresponding electron-ion temperature equilibration time, i.e. the time at which electrons and ions reach thermal equilibrium with the same temperature, is longer by a factor $m_{\rm i}/2m_{\rm e}$ (see Eq. (3.55) of Goedbloed & Poedts 2004). Considering the Fe ions, we obtain that the temperature equilibration time is ≈388 s.

Therefore, in principle, if the electron beam persists for such timescales, the ions could possibly be heated by impacting electrons to temperatures of the electron high-energy tail. However, we remind the reader that the temperature of the $\kappa \approx 2$ high-energy tail is not well-constrained from *RHESSI*.

Finally, we estimate the amount of energy that could be transferred to the ions from the impacting high-energy electron tail. To do so, we calculate the amount $\delta E_{\rm e}$ of the energy contained in the tail. This can be done by integrating the corresponding *RHESSI* spectral component, resulting in $\delta E_{\rm e}/\delta t = 3.7 \times 10^{28}$ erg s^{-1}. The corresponding temperature gain by particular ions can then be estimated as

$$\Delta T_{\rm i} \sim \frac{\delta E_{\rm e}}{\delta t} \frac{\Delta t A_{\rm Fe}}{N_{\rm e} V k_{\rm B}}\,, \tag{14}$$

where Δt is the duration of the high-energy tail, $A_{\rm Fe}$ is the iron abundance, and V is the ambient volume, where the energy exchange occurs. Using the photospheric value of $A_{\rm Fe} \approx 3.2 \times 10^{-5}$ (Asplund et al. 2009), estimating V from the size of the *RHESSI* thermal source at 9–12 keV as $V \approx 2.7 \times 10^{26}$ cm^3, and using $\Delta t = 11$ min as an upper-limit estimate from the *Fermi* lightcurves (see also Long et al. 2018), we obtain $\Delta T_{\rm i} = 0.05$ MK. This value is too low for ambient ions to be efficiently heated by the high-energy electron tail. The value could be increased only by considering that the ambient volume V is much smaller; however, decreasing it by even two orders of magnitude would still produce inefficient heating. We therefore conclude that this mechanism is not a likely explanation of the observed ion emission line profiles.

7. SUMMARY

We reported on the *Hinode*/EIS observations of wide and non-Gaussian profiles of Fe XXIV EUV lines during the impulsive phase of the 2017 September 10 X8.3–class solar flare. These lines are the hottest observed by EIS. We speculate that such a strong departure from Gaussian profiles in the high temperature lines could be observed in this large flare event (and not in previous X-class flares observed by EIS) thanks to the combination of: (1) very intense line profiles, with wings that could be properly fitted; (2) the ideal location of the flare on the limb, which allowed us to observe the high temperature emission in the plasma sheet without contamination from the loop emission; (3) the favorable position of the EIS slit above the flare loops.

The profiles of the Fe XXIV lines could be reliably fitted with a κ-distribution with low values of κ, in the range of $\approx$1.7–3.3. Different κ-values provide information about the number of particles in the high-energy tail (see e.g. Oka et al. 2013, Fig.1).For instance, an electron distribution with κ=2 means that $\approx$ 35% of the particles are accelerated and they carry $>$ 80% of the energy. The non-Gaussian line profiles were found in the location of the top of the flare arcade as observed by *SDO*/AIA in boxes 1 and 2 of Fig. 2, at the bottom and along the plasma sheet feature at about 15:59 UT respectively. The location in box 1 is coincident with the maximum intensity of the *RHESSI* thermal and non-thermal sources at energies of 6 to 300 keV, and is consistent with the location of the EOVSA microwave gyrosynchrotron source at the high-frequency end.

In all the observed profiles, single κ fits of the Fe XXIV 255.10 Å line perform significantly better than single Gaussian fits. On the other hand, the pronounced wings of the Fe XXIV 192.06 Å line profiles can in principle be approximated by multiple-Gaussian fits. However, with only a singular exception, such fits are unconstrained. For the Fe XXIV 255.1 Å line, this is at least in part due to it red wing occurring outside of the corresponding wavelength windows. Nevertheless, a multiple Gaussian fit gives a width for the dominant Fe XXIV 192.06 Å component which is unrealistically narrower ($w_{\rm G}$ = 0.10$\pm$0.005 Å or $FWHM_{\rm G}$ = 0.21$\pm$0.04 Å) than the one obtained in the same location for the other Fe XXIV line at 255.10 Å ($w_{\rm G}$ = 0.13$\pm$0.009 Å or $FWHM_{\rm G}$ = 0.31$\pm$0.02 Å).

Considering different possibilities, we show that the observed non-Gaussian line profiles could either be due to local and continuous ion acceleration, or turbulence. This conclusion is in agreement with Jeffrey et al. (2017). The explanation due to multithermal plasma is unlikely, as the equivalent ion temperatures required by the double-Gaussian fits are unrealistically large. Similarly, although the line profiles have similar κ as the *RHESSI* high-energy tail, as well as possibly similar temperatures, it is unlikely that the electron beam heats these ions, as the energy content of the beam is too weak.

We note that the κ parameter for electrons cannot be diagnosed from line intensities using the ratio-ratio method (cf., Dudík et al. 2014, 2015). We could only use the temperature-sensitive Fe XXIV / Fe XXIII line intensity ratio to diagnose the $T_{\rm e}$, if a value of κ was assumed. This theoretical temperature-sensitive ratio is shifted to larger $T_{\rm e}$ for low κ, a consequence of the behavior of the ionization equilibrium. Using the observed Fe XXIV / Fe XXIII ratio, we obtain $T_{\rm e} = 27$ MK if a Maxwellian distribution is assumed, while for $\kappa = 3$, the temperature reaches 39 MK, and for $\kappa = 2$ it reaches 66 MK. Although this effect leads to an increase of the corresponding thermal velocity for the low κ values determined from line profiles or the *RHESSI* high-energy tail, the line profiles are still broad enough to indicate that the approximate lower limit of the non-thermal velocities, if interpreted in terms of turbulence, can be larger than 200 km s^{-1}.

We conclude that the non-thermal widths, long observed at the start and impulsive phases of solar flares, are likely connected with extremely non-Gaussian line profiles of the hottest Fe lines, which could be detected here due to good wavelength coverage and resolution of EIS. The present observation of the wide non-Gaussian profiles and HXR/microwave loop-top sources, along with the favorable limb geometry of our flare, provide important observational constraints into the mechanisms responsible for the energy release in the impulsive phase of large solar flares.

The authors acknowledge helpful discussions with M. Karlický, G. Del Zanna, and H.E. Mason. J.K. would like to thank the *RHESSI* team, namely K. Tolbert, B. Dennis, S. Krucker and R. Schwartz, for their invaluable advice and software support. V.P. is supported by NASA grant NNX15AF50G, grant number 2015-065 from the University of Alabama in Huntsville and by contract 8100002705 from Lockheed-Martin to SAO. P.T. acknowledges support by NASA grant NNX15AF50G, contract 8100002705 from Lockheed-Martin to SAO, and contract NNM07AB07C to SAO.

J.D., J.K., and E.Dz. acknowledge support from Grants No. 17-16447S and 18-09072S of the Grant Agency of the Czech Republic, as well as institutional support RVO:67985815 from the Czech Academy of Sciences. B.C. acknowledges support by NASA grant NNX17AB82G and NSF grant AGS-1654382. V.P., J.K. and K.K.R. would like to thank the International Space Science Institute (ISSI) for their support and hospitality during the meetings of the ISSI Bern-Bejing team on "Diagnosing heating mechanisms in solar flares through spectroscopic observations of flare ribbons". AIA data are courtesy of NASA/*SDO* and the AIA science team. *Hinode* is a Japanese mission developed and launched by ISAS/JAXA, with NAOJ as domestic partner and NASA and STFC (UK) as international partners. It is operated by these agencies in cooperation with ESA and NSC (Norway). CHIANTI is a collaborative project involving the NRL (USA), the University of Cambridge (UK), and George Mason University (USA).

REFERENCES

Antonucci, E. 1989, Sol. Phys., 121, 31
Antonucci, E., Rosner, R., & Tsinganos, K. 1986, ApJ, 301, 975
Antonucci, E., Gabriel, A. H., Acton, L. W., et al. 1982, Sol. Phys., 78, 107
Asplund, M., Grevesse, N., Sauval, A. J., & Scott, P. 2009, ARA&A, 47, 481
Bamba, Y., Lee, K.-S., Imada, S., & Kusano, K. 2017, ApJ, 840, 116
Battaglia, M., & Kontar, E. P. 2013, ApJ, 779, 107

Battaglia, M., Motorina, G., & Kontar, E. P. 2015, ApJ, 815, 73
Bian, N. H., Emslie, A. G., Stackhouse, D. J., & Kontar, E. P. 2014, ApJ, 796, 142
Boerner, P., Edwards, C., Lemen, J., et al. 2012, Sol. Phys., 275, 41
Brooks, D. H., & Warren, H. P. 2016, ApJ, 820, 63
Brosius, J. W. 2013, ApJ, 777, 135
Caspi, A., & Lin, R. P. 2010, ApJ, 725, L161
Caspi, A., Shih, A. Y., McTiernan, J. M., & Krucker, S. 2015, ApJ, 811, L1
Che, H., & Goldstein, M. L. 2014, ApJ, 795, L38
Culhane, J. L., Rapley, C. G., Bentley, R. D., et al. 1981, ApJ, 244, L141
Culhane, J. L., Harra, L. K., James, A. M., et al. 2007, Sol. Phys., 243, 19
De Pontieu, B., McIntosh, S., Martinez-Sykora, J., Peter, H., & Pereira, T. M. D. 2015, ApJ, 799, L12
De Pontieu, B., Title, A. M., Lemen, J. R., et al. 2014, Sol. Phys., 289, 2733
Del Zanna, G. 2008, A&A, 481, L69
—. 2012, A&A, 537, A38
—. 2013, A&A, 555, A47
Del Zanna, G., Berlicki, A., Schmieder, B., & Mason, H. E. 2006, Sol. Phys., 234, 95
Del Zanna, G., Dere, K. P., Young, P. R., Landi, E., & Mason, H. E. 2015, A&A, 582, A56
Del Zanna, G., O'Dwyer, B., & Mason, H. E. 2011, A&A, 535, A46
Dere, K. P., Landi, E., Mason, H. E., Monsignori Fossi, B. C., & Young, P. R. 1997, A&AS, 125, 149
Doschek, G. A., Feldman, U., Kreplin, R. W., & Cohen, L. 1980, ApJ, 239, 725
Doschek, G. A., Kreplin, R. W., & Feldman, U. 1979, ApJ, 233, L157
Dudík, J., Del Zanna, G., Mason, H. E., & Dzifčáková, E. 2014, A&A, 570, A124
Dudík, J., Polito, V., Dzifčáková, E., Del Zanna, G., & Testa, P. 2017a, ApJ, 842, 19
Dudík, J., Mackovjak, Š., Dzifčáková, E., et al. 2015, ApJ, 807, 123
Dudík, J., Polito, V., Janvier, M., et al. 2016, ApJ, 823, 41
Dudík, J., Dzifčáková, E., Meyer-Vernet, N., et al. 2017b, Sol. Phys., 292, 100
Dzifčáková, E., Dudík, J., Kotrč, P., Fárník, F., & Zemanová, A. 2015, ApJS, 217, 14
Dzifčáková, E., Zemanová, A., Dudík, J., & Mackovjak, Š. 2018, ApJ, 853, 158
Feldman, U., Doschek, G. A., Kreplin, R. W., & Mariska, J. T. 1980, ApJ, 241, 1175
Fletcher, L., Dennis, B. R., Hudson, H. S., et al. 2011, Space Sci. Rev., 159, 19
Freeland, S. L., & Handy, B. N. 1998, Sol. Phys., 182, 497
Gary, D. E., Chen, B., Dennis, B. R., et al. 2018, ArXiv e-prints, arXiv:1807.02498
Goedbloed, J. P. H., & Poedts, S. 2004, Principles of Magnetohydrodynamics
Gontikakis, C., Patsourakos, S., Efthymiopoulos, C., Anastasiadis, A., & Georgoulis, M. K. 2013, ApJ, 771, 126
Gordovskyy, M., Browning, P. K., Kontar, E. P., & Bian, N. H. 2013, Sol. Phys., 284, 489
—. 2014, A&A, 561, A72
Hahn, M., & Savin, D. W. 2015, ApJ, 809, 178
Hasegawa, A., Mima, K., & Duong-van, M. 1985, Physical Review Letters, 54, 2608
Jeffrey, N. L. S., Fletcher, L., & Labrosse, N. 2016, A&A, 590, A99
—. 2017, ArXiv e-prints, arXiv:1701.02196
Jeffrey, N. L. S., Hahn, M., Savin, D. W., & Fletcher, L. 2018, ApJ, 855, L13
Jelínek, P., Karlický, M., Van Doorsselaere, T., & Bárta, M. 2017, ApJ, 847, 98
Kamio, S., Hara, H., Watanabe, T., Fredvik, T., & Hansteen, V. H. 2010, Sol. Phys., 266, 209
Karlický, M., & Bárta, M. 2011, ApJ, 733, 107
Kašparová, J., & Karlický, M. 2009, A&A, 497, L13
Kosugi, T., Matsuzaki, K., Sakao, T., et al. 2007, Sol. Phys., 243, 3
Krucker, S., & Lin, R. P. 2008, ApJ, 673, 1181
Krucker, S., Battaglia, M., Cargill, P. J., et al. 2008, A&A Rev., 16, 155
Laming, J. M., & Lepri, S. T. 2007, ApJ, 660, 1642
Landi, E., Feldman, U., Innes, D. E., & Curdt, W. 2003, ApJ, 582, 506
Lee, K.-S., Imada, S., Watanabe, K., Bamba, Y., & Brooks, D. H. 2017, ApJ, 836, 150
Lemen, J. R., Title, A. M., Akin, D. J., et al. 2012, Sol. Phys., 275, 17
Li, D., Li, Y., Su, W., Huang, Y., & Ning, Z. 2018, ApJ, 854, 26
Li, X., Guo, F., Li, H., & Li, G. 2017, ApJ, 843, 21
Lin, R. P., Dennis, B. R., Hurford, G. J., et al. 2002, Sol. Phys., 210, 3
Livadiotis, G. 2017, Kappa distributions: Theory and Applications in Plasmas (Elsevier, Amsterdam, Netherlands)
Livadiotis, G., & McComas, D. J. 2009, Journal of Geophysical Research (Space Physics), 114, 11105
Long, D. M., Harra, L. K., Matthews, S. A., et al. 2018, ApJ, 855, 74
Milligan, R. O. 2011, ApJ, 740, 70
Oka, M., Ishikawa, S., Saint-Hilaire, P., Krucker, S., & Lin, R. P. 2013, ApJ, 764, 6
Oka, M., Krucker, S., Hudson, H. S., & Saint-Hilaire, P. 2015, ApJ, 799, 129
Olbert, S. 1968, in Astrophysics and Space Science Library, Vol. 10, Physics of the Magnetosphere, ed. R. D. L. Carovillano & J. F. McClay, 641
Pesnell, W. D., Thompson, B. J., & Chamberlin, P. C. 2012, Sol. Phys., 275, 3
Polito, V., Reep, J. W., Reeves, K. K., et al. 2016, ApJ, 816, 89
Polito, V., Reeves, K. K., Del Zanna, G., Golub, L., & Mason, H. E. 2015, ApJ, 803, 84
Schmieder, B., Aulanier, G., & Vršnak, B. 2015, Sol. Phys., 290, 3457
Seaton, D. B., & Darnel, J. M. 2018, ApJ, 852, L9
Sigmar, D., & Joyce, G. 1971, Nuclear Fusion, 11, 447. `http://stacks.iop.org/0029-5515/11/i=5/a=006`
Stix, T. H. 1972, Plasma Physics, 14, 367
Tanaka, K., Watanabe, T., Nishi, K., & Akita, K. 1982, ApJ, 254, L59
Testa, P., De Pontieu, B., & Hansteen, V. 2016, ApJ, 827, 99
Tian, H., Li, G., Reeves, K. K., et al. 2014, ApJ, 797, L14
Vasyliunas, V. M. 1968a, J. Geophys. Res., 73, 2839
Vasyliunas, V. M. 1968b, in Astrophysics and Space Science Library, Vol. 10, Physics of the Magnetosphere, ed. R. D. L. Carovillano & J. F. McClay, 622
Veronig, A. M., & Brown, J. C. 2004, ApJ, 603, L117
Vocks, C., Dzifčáková, E., & Mann, G. 2016, A&A, 596, A41
Vocks, C., Mann, G., & Rausche, G. 2008, A&A, 480, 527
Warren, H. P., Brooks, D. H., Ugarte-Urra, I., et al. 2018, ApJ, 854, 122
Warren, H. P., Ugarte-Urra, I., & Landi, E. 2014, ApJS, 213, 11
Woods, M. M., Harra, L. K., Matthews, S. A., et al. 2017, Sol. Phys., 292, 38
Yan, X. L., Yang, L. H., Xue, Z. K., et al. 2018, ApJ, 853, L18
Young, P. R., Doschek, G. A., Warren, H. P., & Hara, H. 2013, ApJ, 766, 127
Young, P. R., Tian, H., & Jaeggli, S. 2015, ApJ, 799, 218